Chemical Science

rsc.li/chemical-science

ROYAL SOCIETY
OF **CHEMISTRY**

EDGE ARTICLE
Liang Deng, Shengfa Ye, Yisong Guo *et al.*
Spin polarization assisted facile C–H activation by an $S = 1$
iron(IV)–bisimido complex: a comprehensive spectroscopic
and theoretical investigation

Check for updates

Spin polarization assisted facile C−H activation by an *S* = 1 iron(IV)−bisimido complex: a comprehensive spectroscopic and theoretical investigation†

Jin Xiong, [a] Qing Liu, [b] Barbara Lavina, [cd] Michael Y. Hu, [c] Jiyong Zhao, [c] Esen E. Alp, [c] Liang Deng, *[b] Shengfa Ye *[e] and Yisong Guo *[a]

High valent iron terminal imido species (Fe=NR) have been shown to be key reactive intermediates in C−H functionalization. However, the detailed structure–reactivity relationship in Fe=NR species derived from studies of structurally well-characterized high-valent Fe=NR complexes are still scarce, and the impact of imido N-substituents (electron-donating *vs.* electron-withdrawing) on their electronic structures and reactivities has not been thoroughly explored. In this study, we report spectroscopic and computational studies on a rare *S* = 1 iron(IV)−bisimido complex featuring trifluoromethyl groups on the imido N-substituents, [(IPr)Fe(NC(CF$_3$)$_2$Ph)$_2$] (**2**), and two closely related *S* = 0 congeners bearing alkyl and aryl substituents, [(IPr)Fe(NC(CMe$_3$)$_2$Ph)$_2$] (**3**) and [(IPr)Fe(NDipp)$_2$] (**1**), respectively. Compared with **1** and **3**, **2** exhibits a decreased Fe=NR bond covalency due to the electron-withdrawing and the steric effect of the N-substituents, which further leads to a pseudo doubly degenerate ground electronic structure and spin polarization induced β spin density on the imido nitrogens. This unique electronic structure, which differs from those of the well-studied Fe(IV)−oxido complexes and many previously reported Fe(IV)−imido complexes, provides both kinetic and thermodynamic advantages for facile C−H activation, compared to the *S* = 0 counterparts.

Introduction

High valent iron–ligand multiple bond species, such as iron–oxido, iron–imido, iron–nitride, and iron–carbene species, have been postulated as the key reactive species in many important oxidative transformations found in biological and abiological pathways, such as C−H functionalization.[1–13] Iron(IV)–oxido (Fe(IV)=O) intermediates have been identified as the key reactive species in cytochrome P450 dependent and non-heme iron dependent oxygenase/oxidase enzymes, allowing for a stunning array of stereo- and regio-specific oxidative transformations.[12,14–17] While other Fe=E species have not been

[a]Department of Chemistry, Carnegie Mellon University, Pittsburgh, Pennsylvania, 15213, USA. E-mail: ysguo@andrew.cmu.edu

[b]State Key Laboratory of Organometallic Chemistry, Shanghai Institute of Organic Chemistry, Chinese Academy of Sciences, Shanghai, 200032, P. R. China. E-mail: deng@sioc.ac.cn

[c]Advanced Photon Source, Argonne National Laboratory, Argonne, Illinois, 60439, USA

[d]Center for Advanced Radiation Sources, University of Chicago, Chicago, Illinois, 60439, USA

[e]State Key Laboratory of Catalysis, Dalian Institute of Chemical Physics, Chinese Academy of Sciences, Dalian 116023, P. R. China. E-mail: shengfa.ye@dicp.ac.cn

† Electronic supplementary information (ESI) available. CCDC 2172442. For ESI and crystallographic data in CIF or other electronic format see DOI: https://doi.org/10.1039/d2sc06273a

directly linked to biological transformations, recent advances in enzyme bioengineering have repurposed iron-dependent oxygenases to perform abiological group transfer (nitrene and carbene transfer) with high-valent Fe=NR and Fe=CR$_2$ species as key reactive intermediates.[3] Thus, it is crucial to understand the geometric and electronic structures of these high valent Fe=E species to establish structure–reactivity relationships and explore their chemical reactivities and applications in catalysis. In recent decades, the structure–reactivity relationship of Fe(IV)=O species, especially in the hydrogen atom transfer (HAT) reactivity, has been significantly advanced through research efforts in model complex synthesis, enzymatic reactive intermediate trapping, geometric and electronic structure characterizations, chemical reactivity studies and theoretical investigations,[6,7,12,18–26] These studies suggest that the HAT reactivity can be enhanced through a higher spin state of the iron center, a higher reduction potential and/or basicity of the oxido ligand and steric effects (the relative orientation of the orbitals of the donor C–H bond and of the acceptor Fe(IV)=O moiety).

Compared to the progress in research on Fe(IV)=O species, the progress on other Fe=E species is much less developed. Among these species, high valent Fe=NR species have garnered significant attention in fields such as enzyme bioengineering,
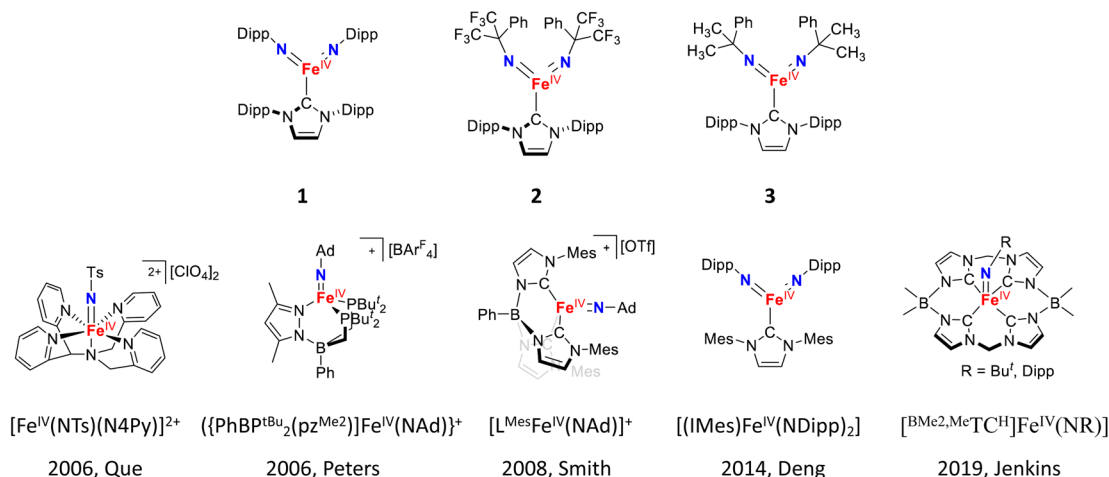
organometallic chemistry and bioinorganic chemistry, as they are thought to be the key reactive intermediates in N_2 reduction, C–H amination, olefin aziridation, and aminohydroxylation.[1,5,27–31] Numerous Fe=NR complexes, including Fe(IV)=NR, Fe(V)=NR, and even Fe(VI)=(NR)$_2$ complexes, have been synthesized.[32–60] However, understanding of the structure–reactivity relationship of iron imido species, derived from studies of structurally well-characterized high-valent Fe=NR complexes, is still limited.

Holland and coworkers have reported crystallographically characterized three-coordinated LFe(III)=NAd complexes (L = a bulky β-diketiminate ligand; Ad = 1-adamantyl).[35–38] Their studies on the HAT reactivity of these Fe(III)–NR have suggested that more exposed imido nitrogen (less steric effect) with high basicity may enhance HAT reactivity.[35,36] Smith and coworkers have also suggested the importance of imido nitrogen basicity on HAT reactivity through studies on a crystallographically characterized four-coordinated Fe(IV)=NAd complex supported by a tris(carbene)-borate ligand.[61] Betley and coworkers have crystallographically characterized three-coordinated $S = 5/2$ dipyrrin supported iron(III)–imido (dipyrrin-Fe(III)=NR (R = Ad, Mes)) complexes and one-electron oxidized four-coordinated iron(III)-iminyl (dipyrrin-FeCl=(˙NR)) complexes that are capable of nitrene transfer and C–H amination.[55,56] Comparative studies on the iron–imido/iminyl redox isomers suggested that a high-spin iron center with strong radical character on the imido nitrogen may improve reaction efficacy in the C–H activation and subsequent amination.[56] These studies suggest that the HAT reactivity of iron–imido species can be promoted by imido nitrogen basicity, iron spin state, and imido nitrogen radical character, thus drawing parallels with iron–oxido species.

Yet, different from the iron–oxido species, iron–imido species display a unique structural feature, namely the presence of N-substituents of the imido ligand. However, the impact of these N-substituents on the electronic structures and reactivities of iron–imido species has not been systemically studied. Based on general chemical principles, electron donating substituents strengthen the Fe=NR bonding interactions, while aromatic or electron withdrawing substituents weaken these interactions by stabilizing the electron lone pair on the imido nitrogen. Such weakening would likely reduce the iron–imido ligand field strength and promote a higher spin state, which may enhance the HAT reactivity. So far, most reported iron–imido complexes bear electron donating or aromatic groups as N-substituents, such as tert-butyl, 1-adamantyl, 2,4,6-trimethylphenyl, 4-tert-butylphenyl, and 2,6-diisopropylphenyl (Dipp) substituents (some examples are shown in Scheme 1).[32–60] Isolable iron–imido species bearing strong electron withdrawing N-substituents are rare.[42,43,45,62–65] Recently, the first structurally characterized Fe(IV)–bisimido complex bearing a strong electron-withdrawing N-substituent, α,α-bis(tri-fluoromethyl)benzyl, was reported by some of us (Scheme 1).[53] The complex, [(IPr)Fe(NC(CF$_3$)$_2$Ph)$_2$] (2, IPr = 1,3-bis(2′,6′-diisopropylphenyl)imidazol-2-ylidene), exhibits an $S = 1$ ground spin state and readily undergoes intramolecular C–H bond dehydrogenation at room temperature via HAT. Interestingly, the replacement of CF$_3$ groups in 2 to electron-donating CH$_3$ groups on the N-substituents resulted in an $S = 0$ Fe(IV)–bisimido complex, [(IPr)Fe(NC(CH$_3$)$_2$Ph)$_2$] (3), which was stable and showed no chemical reactivity even under elevated temperatures (30–70 °C). Additionally, the use of aromatic N-substituents in another similar Fe(IV)–bisimido complex, [(IPr)Fe(Ndipp)$_2$] (1), which would in principle also weaken the Fe=NR bond and promote higher spin state, still yielded an $S = 0$ spin ground state.[48] Thus, complexes 1–3 provide a great opportunity to study the effect of the imido N-substituents on the structure and chemical reactivity of Fe(IV)–imido complexes.

Herein, we present a comprehensive spectroscopic and computational analysis of the novel $S = 1$ complex 2 and its $S = 0$ congeners, 1 and 3. Results from ^{57}Fe nuclear resonance vibrational spectroscopy (NRVS), ^{57}Fe Mössbauer spectroscopy, and direct current (dc) magnetic measurements showed that complex 2 exhibits strongly reduced Fe(IV)=NR bond covalency compared with those of 1 and 3, which leads to distinctive magnetic properties due to its large unquenched orbital angular

Scheme 1 The Fe(IV)–bisimido complexes studied in this work and examples of the previously reported $S = 1$ Fe(IV)–imido complexes.

momentum. We also used the complete-active-space self-consistent field (CASSCF)[66] method combined with N-electron valence state perturbation theory (NEVPT2)[67,68] and DFT calculations to understand the origin of these unique electronic and magnetic properties in **2** and compare them to complexes **1** and **3**. Our findings indicate that the reduction of the Fe(IV)=NR covalency in **2** is not only due to the electron-withdrawing nature of the N-substituents but also due to their steric effects. These two features are not simultaneously present in **1** and **3**. Furthermore, the reduced Fe(IV)=NR covalency in **2** promotes spin polarization that induces β spin density on the imido nitrogens, which facilitates an α spin transfer in the HAT process and is fundamentally different from those in Fe(IV)=O species as well as other Fe(IV)=NR species in a pseudo-C4 ligand field. This unique electronic structure of **2** provides both kinetic and thermodynamic advantages to enable facile C–H activation.

Results and discussion

Structural considerations

The crystal structures of complexes **2** and **3** have been previously reported.[53] Here we present the crystal structure of complex **1** (CCDC: 2172442; see Table S1† for refinement parameters) and highlight key structural differences among **1**, **2** and **3** (Fig. 1). Single-crystal X-ray diffraction experiments revealed that **1** is crystallized in the monoclinic $C2/c$ space group. The Fe atom is three-coordinate with two imido ligands and one N-heterocyclic carbene (NHC) ligand as a spectator ligand. Five major geometric differences can be found among complexes **1–3**. Firstly, the molecular symmetries are different. Complex **1** has a C2 axis along the Fe–C(carbene) bond, resulting in many equivalent molecular metrics, *e.g.* the two Fe=NR bond lengths, the two C–N(imido)–Fe angles, *etc.* Complex **2**, on the other hand, has a C1 symmetry and has two inequivalent Fe=NR bond lengths and two inequivalent C–N(imido)–Fe angles. Secondly, the Fe–ligand bond lengths are generally shorter in **1** when compared with complex **2**. For example, the Fe–C(NHC) bond length is 1.916 Å in **1** but 2.049 Å in **2**; similarly, the Fe–N(imido) bond lengths are 1.638 Å in **1** but 1.705 Å and 1.712 Å in **2**, which is one of the longest Fe–N(imido) bond lengths

reported for iron–imido complexes (Table 2). It is worth noting that the Fe=NR bond is slightly longer in **1** than in **3**, suggesting the expected weakening of this bond *via* an aryl N-substituent. However, the weakening effect is much weaker compared to the electron-withdrawing N-substituents in **2** (see later sections for more discussions). Thirdly, Fig. 1 shows that there is also a difference in the angle between the NHC plane (defined by the 5-membered ring) and the coordination plane (Fe=(NR)₂), which is 35° in **1**, ∼81° in **2**, and ∼4° in **3**. Additionally, the C(imido)–N(imido) = Fe angles and N(imido)=Fe=N(imido) angles are also distinct. The former is almost linear in **1** (173°) and **3** (160–161°) but bent (140–145°) in **2**; the latter is 143° in **1** and ∼125° in both **2** and **3**. This suggests the hybridization mode of N(imido) atom is closer to sp in **1** and **3**, while closer to sp² in **2**. Finally, the angle between the plane of C19–N2=Fe1=N3 and C23–N3=Fe1=N2 (C19–N2···N3–C23 dihedral angle), which controls the relative orientation of two imido nitrogen p orbitals, is also different in these complexes. This angle is 25°, 70°, and ∼0° for **1**, **2**, and **3** respectively. The selected structural metrics of these complexes are listed in Table 1.

⁵⁷Fe nuclear resonance vibrational spectroscopy

To further demonstrate the difference in geometric structures and iron–imido/carbene bonding interactions in these Fe(IV)–bisimido complexes, we conducted ⁵⁷Fe NRVS measurements on **1** and **2** by using polycrystalline samples.[69,70] The ⁵⁷Fe partial vibrational density of states (PVDOS) derived from the NRVS measurements revealed rich vibrational features for complexes **1** and **2** (Fig. 2). The detectable vibrational features extended up to ∼1300 cm⁻¹. We suspect that the features at ∼990 cm⁻¹ and ∼1285 cm⁻¹ observed for complex **1** are vibrational features associated with its Fe(IV)–bisimido moiety. Indeed, earlier IR and Raman investigations on transition metal organoimido complexes showed that vibrations in the energy regions of 900–1100 cm⁻¹ and 1100–1350 cm⁻¹ belong to the vibrations of the M=N–R linkage (M=NR or MN–R stretching).[71] When comparing the ⁵⁷Fe PVDOS data of complex **2** to that of complex **1**, we found all the vibrational features to be red shifted, which is consistent with their differences in Fe–ligand bond lengths (Table 1).
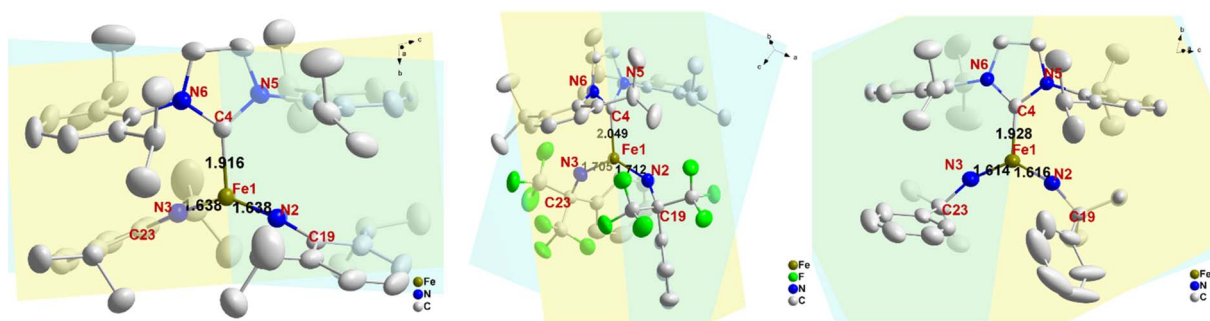

Fig. 1 Thermal ellipsoid plots of complexes **1** (left), **2** (middle), and **3** (right). All the H atoms are omitted. Yellow and blue planes show the NHC ring plane and coordination Fe=(NR)₂ plane. Black numbers show the corresponding Fe–L bond lengths, and the red labels show the atom numbering used in this study.

Table 1 Comparison of the selected structural metrics of complexes **1–3** derived from X-ray crystallographic results

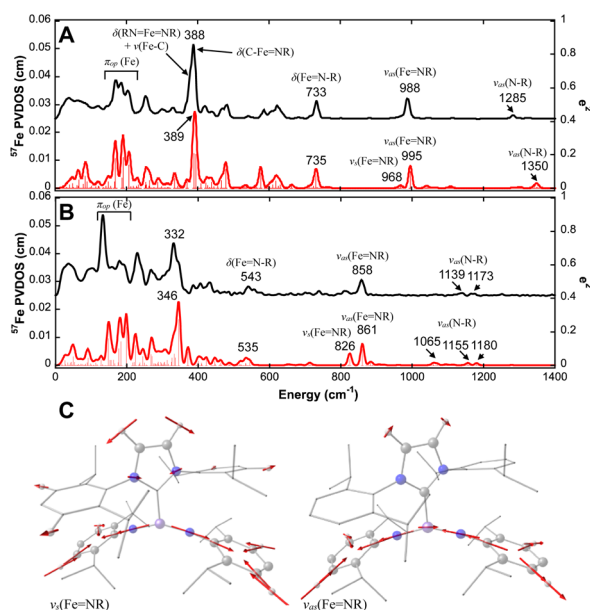|	Complex **1**	Complex **2**	Complex **3**
Bond length (Å)			
Fe=N(imido)	1.638, 1.638	1.705, 1.712	1.614, 1.616
Fe–C(NHC)	1.916	2.049	1.928
N–C(R)	1.376, 1.376	1.438, 1.435	1.440, 1.455
Bond angle (°)			
Fe=N–C(R)	172.68, 172.68	144.05, 140.84	160.16, 161.13
N=Fe=N	142.98	125.28	127.73
N=Fe–C(NHC)	108.51, 108.51	121.22, 113.38	115.59, 116.67
Torsion angle (°)			
N(imido)=Fe–C(NHC)–N(NHC)	35.03, 35.03	78.03, 83.62	−5.79, −2.54
C19–N2···N3–C23	−25.41	−69.69	0.98
Ref.	This work	Ref. 53	Ref. 53

Fig. 2 NRVS-derived ^{57}Fe PVDOS spectra of complexes **1** and **2** and selected normal modes of vibrations. Experimental (black) and DFT-calculated (red) ^{57}Fe PVDOS spectra of **1** (A) and **2** (B) and the symmetric and asymmetric stretching modes of RN=Fe=NR moiety (C) are shown. The frequencies of major spectral features and the mode assignments based on a simplified MX(Y$_2$)$_2$-type molecule are indicated in the figure (see Fig. S4† for mode pictures). The ^{57}Fe PVDOS intensity is shown on the left Y axis while the intensity of calculated mode decomposition factor, e^2, is shown on the right Y axis. The mode pictures in (C) are derived from the DFT frequency calculations of the full structure of complex **1**. The red arrows represent the direction and the magnitude of the atom displacements (>0.07 Å) in the corresponding normal mode of vibration.

To gain a better understanding of the ^{57}Fe PVDOS spectra, we performed DFT calculations. Several functional-basis set combinations were used in the calculations, and all of them reproduced the experimental data reasonably well (Fig. S2 and S3†). Here, the results from the BP86/TZVP[72,73] with GD3 correction[74] are presented in Fig. 2. The DFT optimized structure for complex **1** in an $S = 0$ state and for complex **2** in an $S = 1$

state matched well with their crystal structures (Table S2 and Fig. S1†). Based on the DFT optimized structures, the predicted ^{57}Fe PVDOS spectra of complexes **1** ($S = 0$) and **2** ($S = 1$) derived from frequency calculations also aligned well with the experimental data, allowing us to confidently assign the vibrational modes (see Tables 2 and S4† for a list of vibrational mode assignments and the ESI† for additional analysis and discussion). One key feature revealed by the DFT analysis is that the ^{57}Fe PVDOS features at ~990 cm^{-1} and ~1285 cm^{-1} belong to the vibrations of the M=N–R moieties. The very weak ^{57}Fe PVDOS features at 1285 cm^{-1} and 1322 cm^{-1} (DFT predicted at 1302 and 1350 cm^{-1}) can be assigned to the asymmetric N–R stretching modes between the N and C atoms of the imido ligand (ν_{as}(FeN–R)), which are coupled with different imido substituent vibrations (in this case Dipp vibrations). Due to the short Fe–imido bonds, the asymmetric N–R stretching mode also mixes slightly with the asymmetric Fe=NR stretching mode (ν_{as}(Fe=NR)) to cause the movement of the iron center, thereby rendering their detection. The main ν_{as}(Fe=NR) is located at 988 cm^{-1} (995 cm^{-1} in DFT). The lack of appreciable iron movement in the symmetric Fe=NR stretching mode (ν_s(Fe=NR)) results a weak shoulder at ~970 cm^{-1} (968 cm^{-1} in DFT) for this vibrational mode. In addition, both ν_{as}(Fe=NR) and ν_s(Fe=NR) show strong coupling with aromatic ring vibration from the Dipp substituent (Fig. 3). Overall, the vibrational features of the M=N–R moieties in complex **1** are consistent with many reported metal–imido complexes studied by IR and resonance Raman (Table 2).[75] Furthermore, the NRVS data provided a definitive confirmation for the assignment of the Fe=NR stretching mode and the FeN–R stretching mode, as the former mode leads to stronger iron movement thus higher ^{57}Fe PVDOS intensity than the latter. This is clearly observed in the current NRVS data, showing a high intensity 988 cm^{-1} (ν_{as}(Fe=NR)) and a low intensity 1285 cm^{-1} (ν_{as}(Fe=NR)) features.

For complex **2**, all the vibrational modes identified in complex **1** are shifted to lower frequencies due to the elongation of all the iron–ligand distances in going from **1** to **2** (Fig. 2). In particular, the ν_{as}(Fe=NR) is now located at 858 cm^{-1} (861 cm^{-1} in DFT),

Table 2 Summary of iron–imido stretching vibrations associated with Fe=NR moiety[a]

Complex	d(Fe=NR)	ν(Fe=NR)	ν_{as}(N–R)	Ref.
1	1.638	968 (*968*) s	1285, 1322 (*1302, 1350*) as	This work
		988 (*995*) as		
2	1.709	814 (*826*) s	1139, 1173 (*1060, 1070, 1155, 1180*)	This work
		858 (*861*) as		
$[Fe^{IV}(NTs)(MePy_2tacn)]^{2+}$	1.71	984	—	46
$[Fe^{IV}(NTs)(Me_2CHPy_2tacn)]^{2+}$	1.72	1061	—	46
$[Fe^{IV}(NTs)(N4py)]^{2+}$	1.73	998	—	43
$[(TAML)Fe^{V}(NTs)]^{-}$	1.65	817	—	42
$[PhBP_3]Fe^{III}N^tBu$	1.635	1104	1233	75
$[PhBP_3]Fe^{III}N(1\text{-Ad})$	1.641	1097	1225	75
$[PhBP_3]Fe^{III}NPh$	—	958	1292/1309	75
$[PhBP_3]Fe^{III}N(p\text{-tolyl})$	1.659	962	1281/1305	75
$[Fe_4(\mu_3\text{-}N^tBu)_4(N^tBu)Cl_3]$	1.635	1111	1214	75

[a] The italic numbers are derived from DFT calculations. Distances are in Å, and vibrational frequencies are in cm^{-1}.

the ν_s(Fe=NR) is located at 814 cm^{-1} (826 cm^{-1} in DFT). Thus, the Fe=NR stretching frequency observed for **2** is one of the lowest reported in the literature (Table 2), which is consistent with the relatively long Fe=NR bond length in **2** (1.709 Å). In addition, we compared the displacement of the Fe atom and the N atoms from the bisimido ligands in different normal modes and found that they exhibit a very strong correlation (Fig. S5†). As such, the ^{57}Fe PVDOS spectra of complexes **1** and **2** are dominated by the vibrations associated with Fe–bisimido moiety, which is consistent with the strong Fe=NR bonding interactions in the Fe–bisimido moiety of these two complexes, particularly for complex **1**. Overall, the significantly red-shifted

vibrational frequencies of the Fe=NR and FeN–R stretching modes observed in **2** than those in **1** correlate well with the long Fe=NR bonds in **2**, which further suggests the strongly reduced Fe=NR covalency in this complex.

^{57}Fe Mössbauer spectroscopy and magnetometry

To further study the magnetic properties and electronic structures of complexes **1–3**, we collected variable–temperature–variable–field (VTVH) ^{57}Fe Mössbauer spectra. The low field (0.045 T parallel to the γ-radiation) spectra of **1** (Fig. S6†) and **2** (Fig. 3), measured at 4.2 K, show a single quadrupole doublet,
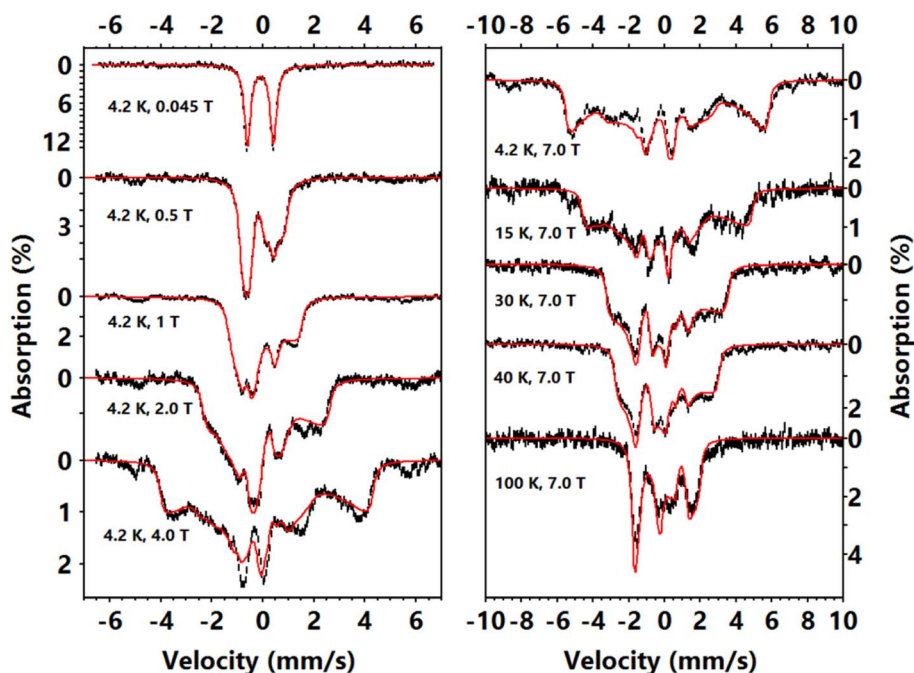

Fig. 3 Mössbauer spectra of complex **2** measured under variant temperatures and external fields. The external field is parallel to the γ-radiation. Black vertical bars show experimental data and their lengths shows the statistical errors. Red lines show the corresponding simulations. Simulation parameters: $S = 1$, $D = -79$ cm^{-1}(fixed), $E/D = 0.085$, $g = [-, -, 2.80]$, $\delta = -0.11$ mm s^{-1}, $\Delta E_Q = -1.02$ mm s^{-1}, $A/g_n\beta_n = [-, -, +35.4]$ T, $\eta = 0$, Euler angles (zyz, V to D) = [0, 90, 0] deg. Exact D, $g_{x'x'}$, $g_{y'y'}$, $A_{x'x'}$ and $A_{y'y'}$ values are undetermined, we use $g_{x'x'} = g_{y'y'} = 2$, $A_{x'x'}/g_n\beta_n = A_{y'y'}/g_n\beta_n = -10.0$ T to generate the present simulating curves.

which is a typical feature of integral spin systems ($S = 0, 1, 2$, …). Complex **1** has an isomer shift (δ) of -0.28 mm s^{-1} and complex **2** has δ of -0.10 mm s^{-1}, similar to other reported Fe(IV)–imido species.[39,48–50,52] The quadrupole splitting (ΔE_Q) of complex **1** is larger than that of complex **2**. The high field spectrum (Fig. S6†) of **1** only shows magnetic splittings due to the externally applied field (7 T), which suggests there is no internal magnetic field in this complex and confirms its diamagnetic nature ($S = 0$). The simulation gives $\Delta E_Q = -1.84$ mm s^{-1} and $\eta = 0.4$. For comparison, the Mössbauer parameters of the diamagnetic complex **3**, which differs from complex **2** by the replacement of –CF$_3$ substituents on the imido ligand with –CH$_3$, were previously reported (at 80 K) as $\delta = -0.41$ mm s^{-1} and $|\Delta E_Q| = 2.40$ mm s^{-1} (the sign of ΔE_Q was not determined).

The VTVH Mössbauer spectra of complex **2** are shown in Fig. 3. The magnetization of the 4.2 K Mössbauer spectra under various applied field is typical of a paramagnetic species with an integer spin ground state, a large negative D ($D \ll 0$), and an easy magnetization direction (an internal field only rapidly develops along the z direction defined by the $\boldsymbol{D}$ tensor, the relative orientations of the $\boldsymbol{D}$, $\boldsymbol{g}$ and electric field gradient (EFG) tensor ($\boldsymbol{V}$) with respect to the molecular frame will be discussed in the electronic structure calculation section below).[76,77] For such a uni-axial magnetic system, the Mössbauer spectra measured at 4.2 K only reflect the properties of the ground non-Kramers doublet of the spin manifold, which can be approximated as an effective $S_{eff} = 1/2$ spin Hamiltonian with $g_{eff,x} = g_{eff,y} \approx 0$, $g_{eff,z} \gg 0$ and an off-diagonal matrix element of the effective spin Hamiltonian $\Delta/2$ (to account for the zero field splitting (Δ) of the magnetic sublevels, see Fig. S7†).[76] With this effective spin Hamiltonian, the VTVH Mössbauer spectra of complex **2** can be satisfactorily simulated (Fig. S8†), which affirms that the ground state electronic structure of **2** indeed features an isolated pseudo-doublet and the excited spin sublevels are not significantly populated even at 100 K.

Overall, the spectral simulations by using the effective spin Hamiltonian revealed two major features: (1) the Mössbauer spectra reveals that a large positive internal field exists in **2** ($B_{int} = -A_{eff,z}\langle S_{eff,z}\rangle/g_n\beta_n \sim +28$ T at 7 T applied field), which indicates the internal field is dominated by the orbital contribution due to the unquenched orbital angular momentum; (2) the largest principal component of the EFG tensor ($V_{z''z}''$) is perpendicular to the direction of the internal field. The obtained effective spin Hamiltonian parameters are $\Delta = 13.6$ cm^{-1}, $g_{eff,z} = 5.6$, $A_{eff,z}/g_n\beta_n = +71$ T, $\Delta E_Q = -1.02$ mm s^{-1}, $\eta = 0$, $V_{z''z}'' \perp g_{eff,z}$, and $\delta = -0.11$ mm s^{-1}. These parameters can be mapped to a canonical $S = 1$ spin Hamiltonian with a large negative D (see Fig. S7†). We can use the $|\pm 1'\rangle$ doublet of an $S = 1$ spin Hamiltonian to mimic the two-level system described by the effective $S_{eff} = 1/2$ spin Hamiltonian. Thus, Δ, $g_{eff,z}$, and $A_{eff,z}$ from the effective Hamiltonian correspond to E, $g_{z'z}'$ and $A_{z'z}'$ of the $S = 1$ Hamiltonian, giving $E = -6.8$ cm^{-1}, $g_{z'z}' = 2.80$, $A_{z'z}'/g_n\beta_n = +35.5$ T (note that x', y', and z' are used to label the x, y and z direction of the $\boldsymbol{D}$, $\boldsymbol{g}$ and $\boldsymbol{A}$ tensors, and to distinguish them from those of the molecular frame coordination, as explained in the electronic structure calculation section). Using

these parameters together with the assumption that the principal axes of $\boldsymbol{A}$ and $\boldsymbol{D}$ are colinear ($A_{z'z}'\|D_{z'z}'$), we were able to obtain the Mössbauer parameters that reproduce all the spectroscopic data of complex **2** with an $S = 1$ spin Hamiltonian (by fixing $D = -79$ cm^{-1} and $\boldsymbol{g} = [2, 2, 2.80]$): $\delta = -0.11$ mm s^{-1}, $\Delta E_Q = -1.02$ mm s^{-1}, $\eta = 0$ with $V_{z''z}'' \perp D_{z'z}'$, $E/D = 0.085$, $A_{z'z}'/g_n\beta_n = +35.5$ T with $A_{z'z}'\|D_{z'z}'$ (Fig. 3).

Dc magnetic measurements were also carried out to further investigate the magnetic anisotropy of **2** (see the analysis in the ESI and Fig. S9† for details). The effective magnetic moment (μ_{eff}) of $\sim 3.1\mu_B$ measured under 300 K and 1 T is larger than spin-only value for a triplet system ($2.832\mu_B$). The VTVH susceptibilities and magnetizations can be well reproduced with the following parameters: $S = 1$, $D = -79$ cm^{-1}, $E/D = 0.077$, $g_\perp = 1.91$, $g_\| = 2.73$, TIP = 1188×10^{-6} emu (TIP refers to temperature-independent paramagnetism). The large D and TIP values are indicative of low-lying excited states and unquenched angular momentum.

Taken together, the magnetic susceptibility/magnetization measurements and the Mössbauer analysis reveal an orbitally nearly degenerate electronic ground state in **2**. In the literature, there are several reported iron complexes exhibiting such an orbitally nearly degenerate electronic structure, but they are either iron(I) or iron(II) species.[47,78–81] To the best of our knowledge, high-valent iron complexes, such as complex **2**, featuring such a unique electronic structure have not been reported yet.

Electronic structure calculations

To elucidate the electronic structures of complexes **1**–**3** and the origin of their spectroscopic properties, highly correlated wavefunction based multi-reference CASSCF/NEVPT2[66–68] calculations were performed using ORCA-5.0.3 program.[82] The selected active space contains 12 electrons distributed across 9 orbitals, including five Fe 3d orbitals and four ligand-based bonding partners, primarily contributed from N(imido) 2p atomic orbitals. To speed up the calculation, truncated molecular fragments were used, with the Dipp substituents replaced by phenyl groups (Fig. 4). The results were discussed using the reference frame shown in the inset of Fig. 4, where the z-axis is defined along the pseudo C3 axis, the y-axis is defined along the Fe–C(carbene) bond, and the x-axis is perpendicular to the yz plane and close to the N(imido)–N(imido) direction.

The *ab initio* calculations show that **1** has a diamagnetic ground state with a leading electron configuration of $(d_{z^2})^2(\pi_{yz}^*)^2(\pi_{xz}^*)^0(\pi_{xy}^*)^0(\pi_{x^2-y^2}^*)^0$, which only accounts for $\sim 73\%$ of the wavefunction, indicating the multi-reference character of the ground state (as shown in Fig. 4). In the leading configuration, d_{z^2} is the doubly occupied non-bonding orbital, while the other four Fe d orbitals participate in π bonding and anti-bonding interactions with p$_y$ and p$_z$ orbitals from the two imido ligands with π_{yz}^* as the other doubly occupied orbital. The calculations yield $\Delta E_Q = -1.75$ mm s^{-1}, $\eta = 0.49$, which are consistent with the Mössbauer simulation for **1**, and the EFG tensor frame is well compatible to the pseudo C_{2v} symmetry, with $V_{z''z}''$ aligning with the z-axis of the molecular frame defined in Fig. 4, $V_{x''x}''$ aligning with y-axis, and $V_{y''y}''$ with x-axis (Fig. S11†).
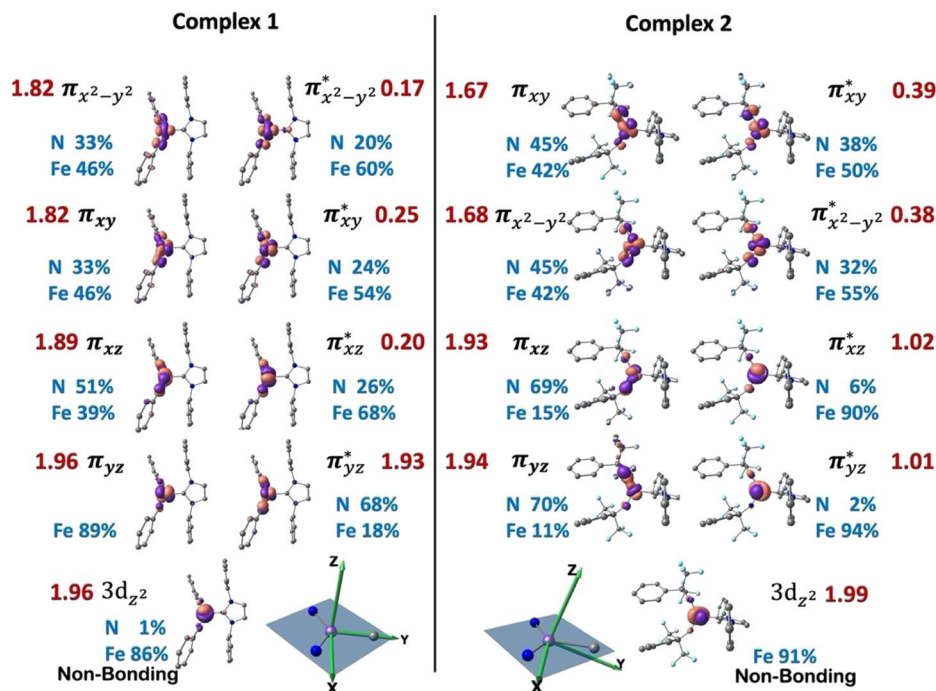
Fig. 4 Natural orbitals and electron configuration of complexes **1** and **2** obtained from ground-state CASSCF(9,12) calculations (contour = 0.1). Labels show the molecular orbital symmetry notations (black), dominant atomic decomposition (blue) and occupation numbers (red). Insert shows the definition of cartesian coordinate frame for 3d orbital decomposition where z direction is defined to be perpendicular to the plane formed by the Fe−(NR)$_2$ moiety. All H atoms are omitted for clarity.

Multi-reference calculations were also performed on **3**, revealing a similar electron ground state as that of complex **1**. Specifically, the leading configuration is the same as **1**, contributing ~75% of the ground state wavefunction. The bonding orbitals π_{xy} and $\pi_{x^2-y^2}$ are heavily mixed and undistinguishable, but the corresponding anti-bonding pairs are well-defined (Fig. S10†). The EFG tensor principal frame also follows the same orientation as that in **1** (Fig. S11†), with the calculated ΔE_Q and η to be −1.81 mm s^{-1} and 0.94, respectively.

The wavefunction of the triplet ground state of **2** exhibits even more substantial multi-reference character, with the leading configuration $(d_{z^2})^2(\pi_{yz}^*)^1(\pi_{xz}^*)^1(\pi_{x^2-y^2}^*)^0(\pi_{xy}^*)^0$ contributing only 59% of the total wavefunction (Fig. 4). This configuration differs greatly from the ground state electron configuration of **1** in that not only a single electron is promoted from π_{yz}^* to π_{xz}^* to lead to a triplet ground state for **2**, more importantly, instead of exhibiting antibonding nature for π_{yz}^* and π_{xz}^* in **1**, these two corresponding orbitals are essentially non-bonding Fe d$_{yz}$ and d$_{xz}$ orbitals in **2** based on orbital decomposition (Fig. 4). This reflects the significant reduction of covalent interactions between iron and the imido ligands in **2**. With three non-bonding orbitals (d$_{z^2}$, d$_{yz}$, and d$_{xz}$) and four 3d electrons, a triplet ground state is favored for **2** based on the first Hund's rule. In addition, the energies of these three non-bonding orbitals are likely to be close, thus leading to an orbital (pseudo)degeneracy. This is confirmed by the excited state calculations. The first triplet excited state with a leading configuration (46%) of $(d_{z^2})^1(\pi_{yz}^*)^2(\pi_{xz}^*)^1(\pi_{x^2-y^2}^*)^0(\pi_{xy}^*)^0$ lies only 1020 cm^{-1} above the ground state. As such, the first excited

state primarily corresponds to a single electron excitation from the d$_{z^2}$ non-bonding orbital of the ground state to the d$_{yz}$ non-bonding orbital, thereby leading to a sizeable unquenched orbital angular momentum along the x-direction. Higher excited states have much larger energy separations from the ground state (Table S4†), thus their spin orbit coupling (SOC) with the ground state is much less pronounced. The calculations give the value of the largest principal component of the $\boldsymbol{g}$ tensor as 2.78, which is much larger than 2, and a large negative D value of −79.2 cm^{-1}. The electronic structure revealed by CASSCF calculations is in agreement with the one reflected by the spectral simulation model: the triplet ground state of complex **2** exhibits a large negative zero-field splitting and strong easy axis magnetic anisotropy. More importantly, the estimated energy separation of 16.2 cm^{-1} for the lowest-energy doublet from the calculations is in a reasonable agreement with $2|E|$ of 13.6 cm^{-1} derived from the spectroscopic simulations. Furthermore, based on the calculations, the direction of the largest principal components ($D_{z''z'}$ and $g_{z''z'}$) of the $\boldsymbol{D}$ and the $\boldsymbol{g}$ tensors, which reflects the direction of unquenched orbital angular momentum, is along the x-direction (Fig. 5). This is consistent with SOC generated by the d$_{yz}$/d$_{z^2}$ pair as described above. Remarkably, the calculations also successfully reproduce the relative orientation between $\boldsymbol{V}$ and $\boldsymbol{D}$ principal axes, with angles of 172° between $V_{z''z'}''$ and D_{yy}', and 97° between $V_{z''z'}''$ and $D_{z'z'}'$, which is consistent with the Mössbauer analysis of **2**.

Finally, the spin density plot shown in Fig. 5 reveals a sizeable negative spin density primarily located in the equatorial plane on two imido N atoms (*i.e.* the RN=Fe=NR coordination
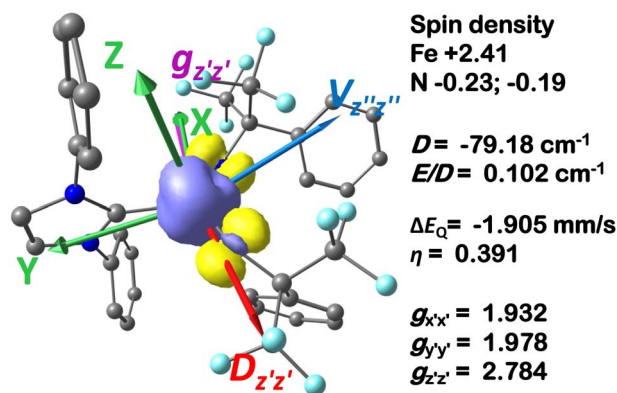
Spin density
Fe +2.41
N -0.23; -0.19

D = -79.18 cm^{-1}
E/D = 0.102 cm^{-1}

ΔE_Q = -1.905 mm/s
η = 0.391

$g_{x'x'}$ = 1.932
$g_{y'y'}$ = 1.978
$g_{z'z'}$ = 2.784

Fig. 5 Ground-state spin density of complex **2** rendered from CASSCF (9,12) calculations (contour = 0.005). The selected tensor axes' orientations as well as calculated tensor principal values are also indicated.

plane). As elaborated in the previous studies for related high-valent iron–nitrido and –oxido complexes,[83,84] the negative spin density is the result of the spin polarization of the formally doubly occupied π_{xy}, and $\pi_{x^2-y^2}$ orbitals induced by the two unpaired electrons resided in the non-bonding Fe d_{xz} and d_{yz} orbitals. As a manifestation, the occupation numbers of formally doubly occupied π_{xy}, and $\pi_{x^2-y^2}$ are considerably less than 2, while those of their correspond antibonding orbitals (π_{xy}^* and $\pi_{x^2-y^2}^*$) are substantially deviated from 0. The drastically reduced covalent interactions between Fe and two imido ligands render the two singly occupied orbitals (Fe d_{xz} and d_{yz}) essentially non-bonding, which leads to a more pronounced spin polarization effect compared to well-studied Fe(IV)–oxido complexes. In the latter complexes Fe is involved in strong covalent interactions with the oxido ligand so that the singly occupied π_{xz}^* of the Fe d_{xz} parentage and π_{yz}^* of the Fe d_{yz} parentage contains substantial contributions from the O-p_x and O-p_y atomic orbitals, thus leading to sizable positive spin population in the O-p_x and O-p_y orbitals and a positive spin density on the oxido ligand. Thus the overall bonding interactions of Fe(IV)=NR moieties in **2** are fundamentally distinct from the well-studied Fe(IV)=O species and the other reported Fe(IV)=NR complexes having a pseudo C4 symmetry. The differences of frontier molecular orbitals (MOs) in complex **1** (or **3**) and **2** derived from CASSCF calculations that show strong covalent interactions between the iron and the imido ligand, as well as those from the well-studied Fe(IV)–oxido complexes are shown in Scheme 2.

Overall, the CASSCF calculations for complexes **1**–**3** successfully reproduced the experimentally determined magnetic spectroscopic parameters. However, since such type of calculations cannot predict Mössbauer isomer shifts, so DFT calculations were performed on the full complex structure to predict this spectroscopic parameter (see the ESI† for detailed computational method). The DFT optimized structures closely resembled the crystal structures of the three complexes (see Table S2 and Fig. S1†). Based on these, isomer shifts were further calculated. Although, the calculated isomer shift

showed a systematic negative shift of ∼0.1 mm s^{-1} from the experimental values based on a published isomer shift calibration method,[85] the overall trend is consistent with the experimental observations, giving a highest isomer shift for complex **2** (−0.19 mm s^{-1}, DFT *vs.* −0.10 mm s^{-1}, exp), a lowest isomer shift for complex **3** (−0.53 mm s^{-1}, DFT *vs.* −0.41 mm s^{-1}, exp), and an isomer shift of −0.42 mm s^{-1} (DFT, *vs.* −0.28 mm s^{-1}, exp) for complex **1** (see Table S5† for the comparison of the calculated and the experimental Mössbauer parameters).
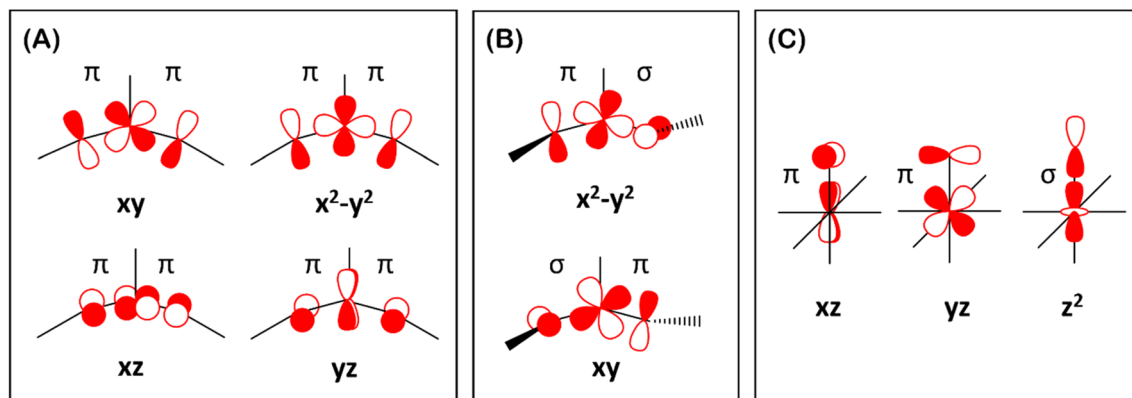
Structure-spin state correlation

To better understand the structural features that result in reduced covalent interactions between Fe and the imido ligands and the stabilization of an $S = 1$ spin state in complex **2**, we carried out a series of DFT calculations. To assess the effect of different structural components on the geometric and electronic structures of the complex, we used a truncated molecular structure derived from the crystal structure of complex **2**. In this truncated structural model, all substituents on NHC and imido ligands were replaced with methyl groups. The geometry optimizations on the truncated model, denoted Me_Me (for the truncated models, nomenclature X_Y is used. X represents the substituents on the NHC ring and Y represents the substituents on the imido ligands) in both $S = 0$ and $S = 1$ states showed that the Fe–ligand bond lengths, the Fe=N–C angles as well as the N=Fe=N bond angles observed in complexes **1** and **2** can be well reproduced (refer to Table S2 and Fig. S12–S14†). This supports the validity of this truncated model for our analysis. In addition, different N-substituents on the imido ligands were further used to construct different truncated models for the calculations to investigate their effects on molecular structure.

According to the CASSCF calculations, the orbital overlap of natural orbitals (NOs) between Fe and the two N(imido) atoms in complexes **1** and **3** is generally excellent as shown in Fig. 4 and S10,† and Scheme 2A. However, in complex **2**, the NOs overlap among these three atoms is significantly reduced due to the unfavorable relative orientation of the Fe 3d and the N(imido) p orbitals (Fig. 4 and Scheme 2B). The Fe 3d orbitals have a good π overlap with the p orbital from only one of the N atoms, leaving a poor σ overlap with the p orbital from the other N atom, thus leading to essentially non-bonding Fe d_{xz} and d_{yz} orbitals (see the π_{xz}/π_{xz}^* and the π_{yz}/π_{yz}^* pair in Fig. 4). Therefore, structural factors that reduce the effective orbital overlap between Fe and the two N atoms are key to stabilize an $S = 1$ state.

Two structural differences between complexes **1** (or **3**) and **2** most likely affect the orbital overlap between Fe and the two N atoms, namely the Fe=N(imido) bond length (1.638 Å in **1**, 1.615 Å in **3**, and 1.709 Å in **2**) and the dihedral angle between the two planes formed by the two Fe–N–C(imido) moieties (C19–N2···N3–C23 dihedral angle, −25° in **1**, 1° in **3**, and −70° in **2**). The tendency to form longer Fe=N bonds in **2** was suggested to be originated from the use of an electron-withdrawing N-substituent, α,α-bis(trifluoromethyl)benzyl. Our DFT calculations support this hypothesis. When using different N-

Scheme 2 Orbital schemes showing the orbital interactions between Fe d orbitals and the imido/oxido ligand p orbitals. (A) the scheme for the S = 0 Fe(IV)−bisimido complexes **1** and **3**; (B) the scheme for the S = 1 Fe(IV)−bisimido complex **2**; and (C) the scheme for the S = 1 Fe(IV)−oxido complexes.

substituents to carry out DFT geometry optimizations on the truncated model, it is evident that alkyl electron-withdrawing N-substituents tend to elongate the Fe=N bonds, regardless of the spin state used, when compared with N–Me (Fig. 6, Table S2†). At the same time, the aryl N-substituents tend to elongate the Fe=N bonds in the singlet state and to a lesser extend in the triplet state. These observations are consistent with the understanding that both electron-withdrawing alkyl and aryl substituents can stabilize the lone pair electrons on the p orbitals of the imido N, thereby weakening the Fe=N bonds. However, based on the DFT calculations on the truncated models, this effect only elongates the Fe=N bonds by a small amount (<0.03 Å), and may not promote the spin state conversion on its own.

The second structural feature that affects the orbital overlap between Fe and the two N atoms is the C19–N2···N3–C23 dihedral angle (see Fig. 1 for atom labeling). For complex **2**, this angle is −70°, which leads to overlap mismatch between the Fe 3d orbitals and N(imido) p orbitals, particularly between d_{xz} and p_z of N(imido), and between d_{xy} and p_y of N(imido), thereby weakening the covalent interactions between Fe and the imido
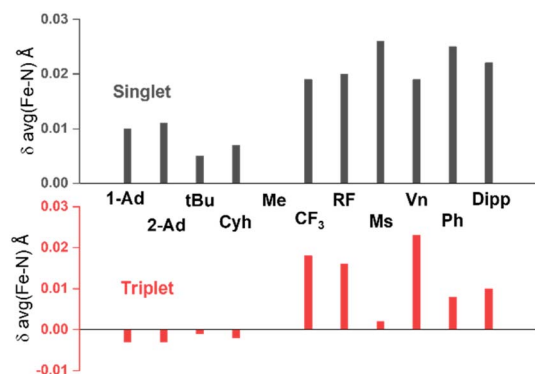

Fig. 6 Imido-substituent-dependent deviation of average Fe−N(imido) distance relative to that of the methyl substituent obtained from DFT optimization. The substituents on NHC side are two methyl groups in all cases presented here. Full data can be found in Table S2.† Abbreviations: Ad = adamantyl, tBu = $tert$-butyl, Cyh = cyclohexyl, RF=C(CF$_3$)$_3$, Ms = methylsulfonyl, Vn = vinyl, Ph = phenyl.

ligands (Scheme 2). This angle is likely to be controlled by steric interactions of the substituents. To provide evidence, we performed geometric scans along the C19–N2···N3–C23 dihedral angle on three truncated models, Me_Me, Me_tBu, and Me_CF$_3$, in the S = 1 state. During scans, the values of other selected key bond lengths and angles were fixed at the crystal structure values from complex **2** (see the ESI† for details). The use of N–Me led to the identification of two local energy minima, with the dihedral angle of ±70° (Fig. 7), which is close to the angle observed in complex **2**. Compared with a 0 degree dihedral angle, the 70 degree angle was favored by ∼2 kcal mol^{-1}. When the bulkiness of the N-substituent was increased from N–Me to N–tBu, 65 degree dihedral angle was favored, with stronger stabilization (by ∼8 kcal mol^{-1}). For N–CF$_3$ substituent, 85 degree dihedral angle was favored, with stabilization of ∼7 kcal mol^{-1}. Therefore, regardless of the nature of N-substituent (electron withdrawing $vs.$ electron donating), its bulkiness favored a large C19–N2···N3–C23 dihedral angle, thus contributing to the mismatch of the orbital overlap between Fe and the two N atoms. Based on this analysis, we reason that the bulkier –CF$_3$ moieties in **2** compared to the –CH$_3$ moieties in **3** likely provide the needed steric effect to favor the large C19–N2···N3–C23 dihedral angle (−70° in **2** $vs.$ 1° in **3**, Fig. 1). The aryl N-substituents (Dipp) in complex **1**, although bulky, form good π–π interactions with the Dipp substituents on the NHC ligand, thus preventing the formation of a large C19–N2···N3–C23 dihedral angle (−25° in **1**, Fig. 1).

Overall, the DFT results suggest that the combination of the N-substituent's steric properties and electron-withdrawing nature reduce the covalent interactions between Fe and the imido ligands in **2**. As also revealed by the CASSCF calculations, this reduction in covalent interactions results in three close lying non-bonding Fe 3d based orbitals (d_{z^2}, d_{yz}, and d_{xz}), which stabilize an S = 1 ground spin state and lead to an orbital pseudo-degeneracy for **2**.

Towards the HAT reactivity

Based on the previously published reactivity studies, it has been demonstrated that complex **2**, with an S = 1 spin state,
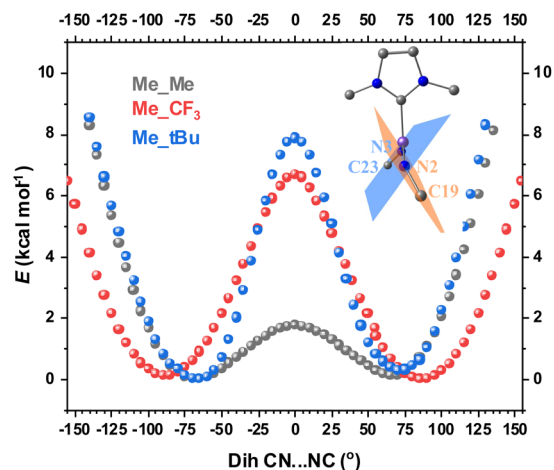
Fig. 7 DFT-assisted partial geometric scan on the dihedral angle C19–N2···N3–C23 to explore the correlation between the steric bulkiness of the N-substituents and the electronic energy of the truncated structural models. The truncated molecular structure in the figure highlights the C–N···N–C dihedral angle, which is the angle between the blue and the orange planes. Black, red and blue plots represent Me_Me, Me_CF$_3$ and Me_tBu models, respectively. The lowest energy for each structural model is defined as zero in the plot. The scans were performed with fixed the Fe–N/C bond lengths, the angles between NHC and Fe═(NR)$_2$ plane, the Fe═N–C angles and the N═Fe═N angles.

undergoes facile intramolecular dehydrogenation more readily than its $S = 0$ counterparts.[53] According to previous DFT studies, the rate-limiting step for the intramolecular dehydrogenation observed in the Fe(IV)–bisimido complexes was suggested to be HAT, and the $S = 1$ Fe(IV)–bisimido complex was found to have a lower kinetic barrier and an higher driving force for HAT than the $S = 0$ Fe(IV)–bisimido complexes.[53]

According to Bell–Evans–Polanyi principle,[86,87] the driving force for C–H activation *via* HAT is determined by the difference in the bond dissociation free energies (BDFEs) between the C–H bond activated and the N–H bond formed in the resulting Fe(III)–NHR species in our case. In the Fe(IV)–bisimido complexes studied here, since the target C–H bond is from the same Dipp substituent, the increased driving force of HAT for complex **2** compared to the $S = 0$ complexes is likely only due to the stronger N–H BDFE in the resulting Fe(III)–NHR species derived from **2**. This is supported by our DFT calculations. The N–H BDFE is highest for the Fe(III)–NHR species derived from complex **2**, which is ~15 kcal mol^{-1} and ~10 kcal mol^{-1} greater than the N–H BDFEs of the Fe(III)–NHR species derived from complexes **1** and **3**, respectively (Fig. S16†). To understand the differences in N–H BDFEs, we used the classical thermodynamic cycle, where the diagonal direction represents the single HAT step and the edges represent two stepwise processes: a sequential proton-transfer (PT) to the Fe(IV)–(NR)$_2$ species followed by an electron transfer (ET) to form the final Fe(III)–NHR species or an ET step followed by a PT step to form the same final state (Fig. S15†). The free energies of the PT and the ET steps can be described by pK_a values and reduction potentials (E^0), respectively. By adopting a thermodynamic analysis

proposed by Srnec and coworkers,[88] we performed DFT analysis (see the ESI, Fig. S16, S17, and Tables S6, S7† for details). By defining an effective pK_a (p$K_{a,eff}$, an averaged pK_a value from the pK_a values of the two PT steps in the thermodynamic scheme) and an effective reduction potential (E^0_{eff}, an averaged E^0 value from the two ET steps), we showed that although complex **2** had a reduced p$K_{a,eff}$ compared to those of complexes **1** and **3** due to the use of the electron-withdrawing substituent (~5 and ~7 units reduction calculated in the benzene solvent or 266 mV and 440 mV reduction when converting to electric potential unit), this withdrawing effect led to a significant increase of E^0_{eff} in **2** compared to the other two complexes (613 mV and 882 mV increase respectively). Therefore, the higher reduction potential of complex **2** is likely the dominant factor determining the stronger N–H BDFE of the resulting Fe(III)–NH species than those derived from **1** and **3**, thus making **2** more reactive than the $S = 0$ complexes.

In addition to the HAT driving force, the kinetic barrier of the HAT reaction is equally important. Our CASSCF and DFT calculations suggest that the unique ground state electronic and geometric structures of complex **2** may directly contribute to the lowering of the reaction barrier by mimicking the features of the transition state in the HAT step. The ground state and the transition state structures of complex **2** are highly similar, featuring a large β spin density on the p orbital of imido nitrogen in the RN═Fe═NR coordination plane (Fig. 5, 8, and S18†). This p orbital, which is involved in bonding/antibonding interactions with Fe d$_{xy}$/d$_{x^2-y^2}$ orbitals (see the π_{xy}/π^*_{xy} and the $\pi_{x^2-y^2}$/$\pi^*_{x^2-y^2}$ pair in Fig. 4), points toward the C–H bond to be activated on the Dipp substituent of NHC ligand, providing the necessary orbital overlap to facilitate the initial electron transfer from the C–H bond to the Fe(IV)═NR moiety in the HAT process (Fig. 5 and 8). In addition, the transition state spin density distribution reveals that the initial electron transfer may occur *via* an α spin transfer since the carbon of the C–H bond being activated bears a β spin density (Fig. 8). This α spin transfer may be facilitated by the β spin density on the p orbital of imido nitrogen (Fig. 8). The α spin transfer channel of HAT in **2** resembles the σ pathway in the well-studied Fe(IV)═O complexes, where due to the positioning of the C–H bond relative to the Fe(IV)═O bond vector an α spin transfer to the σ* MO with Fe d$_{z^2}$ parentage occurs in the so-called σ pathway. Additionally, in Fe(IV)═O complexes, a β spin transfer to the singly occupied π* MO with Fe d$_{xz}$/d$_{yz}$ parentage is also possible, which occurs in the π pathway (Schemes 2 and S1†). This dual-channel reactivity does not likely to exist in **2**, since the singly occupied frontier MOs in **2** are essentially non-bonding d$_{xz}$/d$_{yz}$ orbitals (Fig. 4), which exhibit minimal orbital overlap with the C–H bond, thus preventing an efficient β spin transfer during the HAT process. Thus, **2** likely carries out HAT *via* a single α spin transfer channel (Fig. 8).

In summary, the facile C–H activation reactivity of $S = 1$ complex **2** correlates well with its electronic structure, which features a β spin density on the imido nitrogen due to the reduced covalent interactions between Fe and the imido ligands and the strengthened spin polarization effect, an exposed N p orbital of the imido ligand towards the C–H bond due to bent
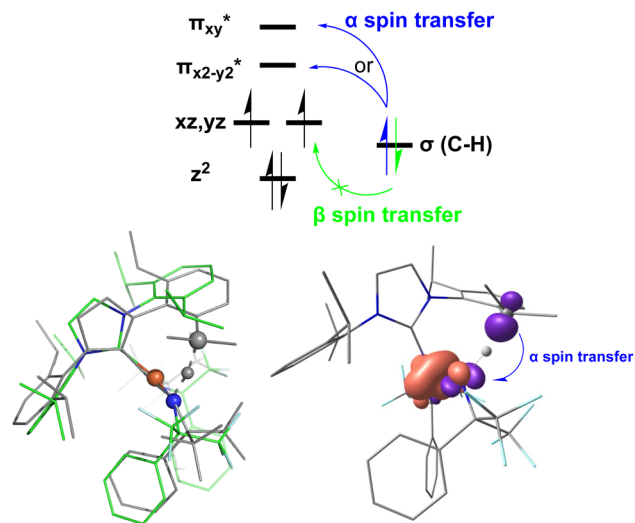
Fig. 8 Electron transfer pathways (top) and the ground state and the transition state structures, and spin density plot derived from DFT calculations of complex **2** (bottom). Top: the scheme of the α spin transfer and the β spin transfer pathways for complex **2**. Bottom: the structural overlay of the DFT optimized ground state (colored) and the transition state (grey) of complex **2**, highlighting the similarity of these two structures and the close vicinity of the imido nitrogen to the C−H bond being activated in both structures (left) and the spin density plot at the transition state, highlighting the α spin transfer in the HAT process (right).

and twisted Fe=N–R angle and C–N···N–C dihedral angle, and an electron-withdrawing N-substituent.

Conclusions

In this study, a rare $S = 1$ Fe(IV)–bisimido complex bearing electron-withdrawing N-substituents, **2**, has been subjected to in-depth structural, spectroscopic (NRVS and Mössbauer), and magnetization studies. These studies were compared to those on two $S = 0$ Fe(IV)–bisimido complexes without electron-withdrawing N-substituents, **1** and **3**. The results showed that the structural and vibrational properties of these complexes are primarily determined by the covalent Fe(IV)–imido bonding interactions. However, complex **2** with an $S = 1$ ground state exhibits significantly reduced covalency, as evidenced by the longer Fe–imido bonds (0.07–0.1 Å longer) and the lower Fe–imido vibration frequencies (>100 cm^{-1} lower) compared to the diamagnetic **1** and **3**. In addition, **2** shows an orbitally nearly degenerate electronic ground state, which leads to a sizeable unquenched orbital angular momentum and a large positive internal magnetic field. The CASSCF/NEVPT2 calculations further elucidated that the unique ground state electronic structure of **2** is due to the spin–orbit coupling to a low-lying excited triplet state corresponding to a single electron excitation from the non-bonding d$_{z^2}$ orbital to the d$_{yz}$ based MO. And the conversion of the singlet **1** (or **3**) to the triplet **2** is the result of the significant reduction in the covalent interactions between iron and the imido nitrogens, which converts the d$_{yz}$ and d$_{xz}$ based π_{yz}^* and π_{xz}^* orbitals in **1** (or **3**) to the non-bonding d$_{yz}$ and

d$_{xz}$ orbitals. With three energetically close-lying iron non-bonding orbitals (d$_{z^2}$, d$_{yz}$, and d$_{xz}$), an $S = 1$ spin state is thus favored. To further explore the structural and electronic factors in controlling the spin state of these Fe(IV)–bisimido complexes, DFT calculations were performed. The results suggested that the steric effect of the N-substituents and their electron-withdrawing nature are two synergistic factors that reduce covalent interactions between Fe and the imido ligands and stabilize the $S = 1$ state for complex **2**. Finally, the ground state electronic structure of **2**, derived from structural, spectroscopic, and theoretical investigations, is connected to its chemical reactivity. It was found that the existence of a radical character on the imido nitrogen, an exposed N p orbital of the imido ligand towards the C–H bond to be activated, and the use of an electron-withdrawing N-substituent are key factors that provide both kinetic and thermodynamic advantages over the $S = 0$ counterparts to enable facile C–H activation reactivity. Remarkably, the two singly occupied Fe non-bonding d$_{yz}$ and d$_{xz}$ orbitals exert strong spin-polarization effect that results in a sizable β spin population on the imido nitrogens in **2**, which facilitates the α spin transfer in the HAT process. Thus, complex **2** represents the first identified example of a high valent iron–imido species that conducts HAT via a single α spin transfer reaction channel, distinguishing it from iron(IV)–oxido complexes.

Data availability

Crystallographic data for compound **1** has been deposited at CCDC under accessing number 2172442. The coordinates of DFT optimized structures have been uploaded as part of the supplementary material.

Author contributions

Conceptualization: L. D., S. Y., Y. G.; Methodology, M. Y. H., J. Z., E. E. A., L. D., S. Y., Y. G.; Investigation: J. X.; Q. L.; B. L., M. Y. H., J. Z., E. E. A., L. D., S. Y., Y. G.; Formal Analysis: J. X.; Q. L., L. D., S. Y., Y. G.; Writing – Original Draft: J. X., Y. G.; Writing – Review & Editing, J. X., Q. L., L. D., S. Y., Y. G.; Funding Acquisition: L. D., S. Y., Y. G.

Conflicts of interest

There are no conflicts to declare.

Acknowledgements

Notes and references

1 M. P. Mehn and J. C. Peters, *J. Inorg. Biochem.*, 2006, **100**, 634–643.

2 L. Que, *Acc. Chem. Res.*, 2007, **40**, 493–500.

3 N. P. Dunham and F. H. Arnold, *ACS Catal.*, 2020, **10**, 12239–12255.

4 E. I. Solomon, D. E. DeWeese and J. T. Babicz, *Biochemistry*, 2021, **60**, 3497–3506.

5 C.-M. Che, C.-Y. Zhou and E. L.-M. Wong, *Catalysis by Fe=X Complexes (X = NR, CR2) - Iron Catalysis: Fundamentals and Applications*, ed. B. Plietker, Springer, Berlin, Heidelberg, 2011, pp. 111–138.

6 W. Nam, *Acc. Chem. Res.*, 2007, **40**, 522–531.

7 C. Krebs, D. G. Fujimori, C. T. Walsh and J. M. J. Bollinger, *Acc. Chem. Res.*, 2007, **40**, 484–492.

8 J. M. Smith and D. Subedi, *Dalt. Trans.*, 2012, **41**, 1423–1429.

9 J. Hohenberger, K. Ray and K. Meyer, *Nat. Commun.*, 2012, **3**, 720.

10 G. Olivo, O. Cussó, M. Borrell and M. Costas, *J. Biol. Inorg Chem.*, 2017, **22**, 425–452.

11 M. C. White and J. Zhao, *J. Am. Chem. Soc.*, 2018, **140**, 13988–14009.

12 X. Huang and J. T. Groves, *Chem. Rev.*, 2018, **118**, 2491–2553.

13 J. Cheng, L. Wang, P. Wang and L. Deng, *Chem. Rev.*, 2018, **118**, 9930–9987.

14 *2-Oxoglutarate-Dependent Oxygenases*, ed C. Schofield and R. Hausinger, Royal Society of Chemistry, Cambridge, 2015.

15 *Cytochrome P450*, ed. P. R. Ortiz de Montellano, Springer International Publishing, Cham, 4th edn, 2015.

16 Y. Guo, W. Chang, J. Li and M. Davidson, in *Comprehensive Coordination Chemistry III*, ed. E. C. Constable, G. Parkin and L. B. T.-C. C. C. I. I. I. Que Jr, Elsevier, Oxford, 2021, pp. 269–300.

17 Y. Guo, W. Chang, J. Li and M. Davidson, in *Comprehensive Coordination Chemistry III*, eds. E. C. Constable, G. Parkin and L. B. T.-C. C. C. I. I. I. Que Jr, Elsevier, Oxford, 2021, pp. 301–332.

18 J. M. Mayer, *Acc. Chem. Res.*, 2011, **44**, 36–46.

19 J. L. Lee, D. L. Ross, S. K. Barman, J. W. Ziller and A. S. Borovik, *Inorg. Chem.*, 2021, **60**, 13759–13783.

20 M. Puri and L. Que, *Acc. Chem. Res.*, 2015, **48**, 2443–2452.

21 T. H. Yosca, A. P. Ledray, J. Ngo and M. T. Green, *J. Biol. Inorg Chem.*, 2017, **22**, 209–220.

22 M. L. Neidig, A. Decker, O. W. Choroba, F. Huang, M. Kavana, G. R. Moran, J. B. Spencer and E. I. Solomon, *Proc. Natl. Acad. Sci. USA*, 2006, **103**, 12966–12973.

23 B. Mondal, L. Roy, F. Neese and S. Ye, *Isr. J. Chem.*, 2016, **56**, 763–772.

24 S. Shaik, H. Chen and D. Janardanan, *Nat. Chem.*, 2011, **3**, 19–27.

25 S. Shaik, H. Hirao and D. Kumar, *Acc. Chem. Res.*, 2007, **40**, 532–542.

26 M. G. Quesne, A. S. Faponle, D. P. Goldberg and S. P. de Visser, in *Spin States in Biochemistry and Inorganic Chemistry*, ed. M. Swart and M. Costas, John Wiley & Sons, Ltd, Oxford, UK, 2015, pp. 185–202.

27 T. G. Driver, *Org. Biomol. Chem.*, 2010, **8**, 3831–3846.

28 L. Zhang and L. Deng, *Chin. Sci. Bull.*, 2012, **57**, 2352–2360.

29 P. Wang and L. Deng, *Chin. J. Chem.*, 2018, **36**, 1222–1240.

30 Y. Liu, T. You, T.-T. Wang and C.-M. Che, *Tetrahedron*, 2019, **75**, 130607.

31 Y. Liu, T. You, H.-X. Wang, Z. Tang, C.-Y. Zhou and C.-M. Che, *Chem. Soc. Rev.*, 2020, **49**, 5310–5358.

32 A. K. Verma, T. N. Nazif, C. Achim and S. C. Lee, *J. Am. Chem. Soc.*, 2000, **122**, 11013–11014.

33 C. M. Thomas, N. P. Mankad and J. C. Peters, *J. Am. Chem. Soc.*, 2006, **128**, 4956–4957.

34 S. Kuppuswamy, T. M. Powers, B. M. Johnson, M. W. Bezpalko, C. K. Brozek, B. M. Foxman, L. A. Berben and C. M. Thomas, *Inorg. Chem.*, 2013, **52**, 4802–4811.

35 R. E. Cowley and P. L. Holland, *Inorg. Chem.*, 2012, **51**, 8352–8361.

36 R. E. Cowley, N. A. Eckert, S. Vaddadi, T. M. Figg, T. R. Cundari and P. L. Holland, *J. Am. Chem. Soc.*, 2011, **133**, 9796–9811.

37 R. E. Cowley, N. J. DeYonker, N. A. Eckert, T. R. Cundari, S. DeBeer, E. Bill, X. Ottenwaelder, C. Flaschenriem and P. L. Holland, *Inorg. Chem.*, 2010, **49**, 6172–6187.

38 N. A. Eckert, S. Vaddadi, S. Stoian, R. J. Lachicotte, T. R. Cundari and P. L. Holland, *Angew. Chem., Int. Ed.*, 2006, **45**, 6868–6871.

39 M. R. Anneser, G. R. Elpitiya, J. Townsend, E. J. Johnson, X. B. Powers, J. F. DeJesus, K. D. Vogiatzis and D. M. Jenkins, *Angew. Chem., Int. Ed.*, 2019, **58**, 8115–8118.

40 J. A. Bellow, M. Yousif, A. C. Cabelof, R. L. Lord and S. Groysman, *Organometallics*, 2015, **34**, 2917–2923.

41 S. Hong, X. Lu, Y.-M. Lee, M. S. Seo, T. Ohta, T. Ogura, M. Clémancey, P. Maldivi, J.-M. Latour, R. Sarangi and W. Nam, *J. Am. Chem. Soc.*, 2017, **139**, 14372–14375.

42 S. Hong, K. D. Sutherlin, A. K. Vardhaman, J. J. Yan, S. Park, Y. Lee, S. Jang, X. Lu, T. Ohta, T. Ogura, E. I. Solomon and W. Nam, *J. Am. Chem. Soc.*, 2017, **139**, 8800–8803.

43 E. J. Klinker, T. A. Jackson, M. P. Jensen, A. Stubna, G. Juhász, E. L. Bominaar, E. Münck and L. Que Jr, *Angew. Chem., Int. Ed.*, 2006, **45**, 7394–7397.

44 S. D. Brown and J. C. Peters, *J. Am. Chem. Soc.*, 2004, **126**, 4538–4539.

45 P. Leeladee, G. N. L. Jameson, M. A. Siegler, D. Kumar, S. P. de Visser and D. P. Goldberg, *Inorg. Chem.*, 2013, **52**, 4668–4682.

46 G. Sabenya, I. Gamba, L. Gómez, M. Clémancey, J. R. Frisch, E. J. Klinker, G. Blondin, S. Torelli, L. Que, V. Martin-Diaconescu, J.-M. Latour, J. Lloret-Fillol and M. Costas, *Chem. Sci.*, 2019, **10**, 9513–9529.

47 J. Cheng, J. Liu, X. Leng, T. Lohmiller, A. Schnegg, E. Bill, S. Ye and L. Deng, *Inorg. Chem.*, 2019, **58**, 7634–7644.

48 L. Wang, L. Hu, H. Zhang, H. Chen and L. Deng, *J. Am. Chem. Soc.*, 2015, **137**, 14196–14207.

49 H. Zhang, Z. Ouyang, Y. Liu, Q. Zhang, L. Wang and L. Deng, *Angew. Chem., Int. Ed.*, 2014, **53**, 8432–8436.

50 K. Searles, S. Fortier, M. M. Khusniyarov, P. J. Carroll, J. Sutter, K. Meyer, D. J. Mindiola and K. G. Caulton, *Angew. Chem., Int. Ed.*, 2014, **53**, 14139–14143.

51 B. P. Jacobs, P. T. Wolczanski, Q. Jiang, T. R. Cundari and S. N. MacMillan, *J. Am. Chem. Soc.*, 2017, **139**, 12145–12148.

52 J. L. Martinez, S. A. Lutz, H. Yang, J. Xie, J. Telser, B. M. Hoffman, V. Carta, M. Pink, Y. Losovyj and J. M. Smith, *Science*, 2020, **370**, 356–359.

53 Q. Liu, L. Long, P. Ma, Y. Ma, X. Leng, J. Xiao, H. Chen and L. Deng, *Cell Rep. Phys. Sci.*, 2021, **2**, 100454.

54 S. D. Brown, T. A. Betley and J. C. Peters, *J. Am. Chem. Soc.*, 2003, **125**, 322–323.

55 M. J. T. Wilding, D. A. Iovan and T. A. Betley, *J. Am. Chem. Soc.*, 2017, **139**, 12043–12049.

56 M. J. T. Wilding, D. A. Iovan, A. T. Wrobel, J. T. Lukens, S. N. MacMillan, K. M. Lancaster and T. A. Betley, *J. Am. Chem. Soc.*, 2017, **139**, 14757–14766.

57 D. A. Iovan and T. A. Betley, *J. Am. Chem. Soc.*, 2016, **138**, 1983–1993.

58 E. T. Hennessy, R. Y. Liu, D. A. Iovan, R. A. Duncan and T. A. Betley, *Chem. Sci.*, 2014, **5**, 1526–1532.

59 E. T. Hennessy and T. A. Betley, *Science*, 2013, **340**, 591–595.

60 E. R. King, E. T. Hennessy and T. A. Betley, *J. Am. Chem. Soc.*, 2011, **133**, 4917–4923.

61 I. Nieto, F. Ding, R. P. Bontchev, H. Wang and J. M. Smith, *J. Am. Chem. Soc.*, 2008, **130**, 2716–2717.

62 A. K. Vardhaman, P. Barman, S. Kumar, C. V Sastri, D. Kumar and S. P. de Visser, *Angew. Chem., Int. Ed.*, 2013, **52**, 12288–12292.

63 S. Kumar, A. S. Faponle, P. Barman, A. K. Vardhaman, C. V Sastri, D. Kumar and S. P. De Visser, *J. Am. Chem. Soc.*, 2014, **136**, 17102–17115.

64 G. Mukherjee, F. G. C. Reinhard, U. K. Bagha, C. V Sastri and S. P. de Visser, *Dalt. Trans.*, 2020, **49**, 5921–5931.

65 D. M. Spasyuk, S. H. Carpenter, C. E. Kefalidis, W. E. Piers, M. L. Neidig and L. Maron, *Chem. Sci.*, 2016, **7**, 5939–5944.

66 B. O. Roos, *Adv. Chem. Phys.*, 1987, 399–445.

67 C. Angeli, R. Cimiraglia, S. Evangelisti, T. Leininger and J.-P. Malrieu, *J. Chem. Phys.*, 2001, **114**, 10252–10264.

68 C. Angeli, R. Cimiraglia and J.-P. Malrieu, *J. Chem. Phys.*, 2002, **117**, 9138–9153.

69 J. T. Sage, C. Paxson, G. R. a Wyllie, W. Sturhahn, S. M. Durbin, P. M. Champion, E. E. Alp and W. R. Scheidt, *J. Phys. Condens. Matter*, 2001, **13**, 7707–7722.

70 W. Sturhahn, *J. Phys. Condens. Matter*, 2004, **16**, S497–S530.

71 D. E. Wigley, *Prog. Inorg. Chem.*, 1994, 239–482.

72 A. D. Becke, *Phys. Rev. A*, 1988, **38**, 3098–3100.

73 J. P. Perdew, *Phys. Rev. B: Condens. Matter Mater. Phys.*, 1986, **33**, 8822–8824.

74 S. Grimme, J. Antony, S. Ehrlich and H. Krieg, *J. Chem. Phys.*, 2010, **132**, 154104.

75 M. P. Mehn, S. D. Brown, D. M. Jenkins, J. C. Peters and L. Que, *Inorg. Chem.*, 2006, **45**, 7417–7427.

76 H. Andres, E. L. Bominaar, J. M. Smith, N. A. Eckert, P. L. Holland and E. Münck, *J. Am. Chem. Soc.*, 2002, **124**, 3012–3025.

77 B. M. Hakey, D. C. Leary, J. Xiong, C. F. Harris, J. M. Darmon, J. L. Petersen, J. F. Berry, Y. Guo and C. Milsmann, *Inorg. Chem.*, 2021, **60**, 18575–18588.

78 J. M. Zadrozny, D. J. Xiao, M. Atanasov, G. J. Long, F. Grandjean, F. Neese and J. R. Long, *Nat. Chem.*, 2013, **5**, 577–581.

79 M. Atanasov, J. M. Zadrozny, J. R. Long and F. Neese, *Chem. Sci.*, 2013, **4**, 139–156.

80 M. Keilwerth, J. Hohenberger, F. W. Heinemann, J. Sutter, A. Scheurer, H. Fang, E. Bill, F. Neese, S. Ye and K. Meyer, *J. Am. Chem. Soc.*, 2019, **141**, 17217–17235.

81 M. Tarrago, C. Römelt, J. Nehrkorn, A. Schnegg, F. Neese, E. Bill and S. Ye, *Inorg. Chem.*, 2021, **60**, 4966–4985.

82 F. Neese, F. Wennmohs, U. Becker and C. Riplinger, *J. Chem. Phys.*, 2020, **152**, 224108.

83 B. Mondal, F. Neese, E. Bill and S. Ye, *J. Am. Chem. Soc.*, 2018, **140**, 9531–9544.

84 H.-C. Chang, B. Mondal, H. Fang, F. Neese, E. Bill and S. Ye, *J. Am. Chem. Soc.*, 2019, **141**, 2421–2434.

85 M. Römelt, S. Ye and F. Neese, *Inorg. Chem.*, 2009, **48**, 784–785.

86 R. P. Bell, *Proc. R. Soc. London, Ser. A*, 1936, **154**, 414–429.

87 M. G. Evans and M. Polanyi, *Trans. Faraday Soc.*, 1938, **34**, 11–24.

88 D. Bím, M. Maldonado-Domínguez, L. Rulíšek and M. Srnec, *Proc. Natl. Acad. Sci. USA*, 2018, **115**, E10287–E10294.